applied sciences

MDPI

Article

Calibration of a 3-Component External Balance for MAVs Wind Tunnel Research

Rafael Bardera [1,*], Ángel Antonio Rodriguez-Sevillano [2], Estela Barroso Barderas [1], Suthyvann Sor [1] and Juan Carlos Matías García [1]

[1] Instituto Nacional de Técnica Aeroespacial (INTA), 28850 Torrejón de Ardoz, Spain; barrosobe@inta.es (E.B.B.); sors@inta.es (S.S.); matiasgjc@inta.es (J.C.M.G.)
[2] Escuela Técnica Superior de Ingeniería Aeronáutica y del Espacio, Universidad Politécnica de Madrid, 28040 Madrid, Spain; angel.rodriguez.sevillano@upm.es
* Correspondence: barderar@inta.es

Abstract: This paper presents a 3-component external balance, specifically designed, built, and calibrated at the National Institute for Aerospace Technology (INTA) for measuring aerodynamic forces on Micro Aerial Vehicles in the wind tunnel. The balance employs high-precision strain gauge cells as its load-sensing elements, strategically positioned in a metallic structure to measure lift force, aerodynamic drag force, and pitching moment. The entire calibration process of the balance, including the mathematical formulation to derive the calibration matrix and the calibration bench designed and manufactured for this purpose, is detailed in this paper. Moreover, the complete analysis of component interferences of the aerodynamic components and an assessment of the uncertainties inherent in the system are presented.

Keywords: external balance; calibration; measurement

Citation: Bardera, R.; Rodriguez-Sevillano, Á.A.; Barroso Barderas, E.; Sor, S.; Matías García, J.C. Calibration of a 3-Component External Balance for MAVs Wind Tunnel Research. *Appl. Sci.* **2024**, *14*, 11236. https://doi.org/10.3390/app142311236

Received: 13 October 2024
Revised: 8 November 2024
Accepted: 15 November 2024
Published: 2 December 2024

1. Introduction

A wind tunnel balance is a highly engineered and adaptable structural device specifically designed to measure aerodynamic loads on a scale model during wind tunnel testing. In their study, Gonzalez et al. [1] provide an extensive overview of these devices in Fluid Mechanics, offering insights into their types, components, and calibration techniques. These balances are typically divided into the following two primary categories: internal and external, based on their placement within the test setup. An internal balance is embedded within the model, while an external balance operates outside the model or test section [2].

External balances come in either multi-piece or one-piece configurations. The one-piece balance is tailored to measure aerodynamic loads in half-model tests [3,4], whereas a multi-piece balance consists of separate force transducers linked together by a framework [5]. Positioned outside the model or test section, external balances can be optimized for various requirements, such as enhanced sensitivity, stiffness, and the decoupling of load interactions [6].

The accuracy and reliability of wind tunnel balance measurements are influenced by several factors. A well-thought-out design and meticulous calibration process are key elements in ensuring the device's performance. Selecting the most suitable balance type and tailoring its components to the specific testing requirements are fundamental to achieving accurate and repeatable measurements [7]. For example, the Institute of Aeronautics and Space in Brazil employs a specialized external balance equipped with six strain gauge load cells, which allows for precise measurements in both subsonic and transonic wind tunnel facilities. These balances are also widely used in full-scale automobile testing, highlighting their versatility and importance in a wide range of aerodynamic studies [8].

Another in-depth resource on wind tunnel balances and their applications can be found in [9–13]. Morris [10] and Raush [11] focus on the development of force balance systems

specifically for educational wind tunnels. They use a design approach using flexible rods for measuring forces in wind tunnels that will enhance sensitivity and flexibility, making it suitable for educational purposes. Vadassery [12] described the fabrication and testing of an external balance for measuring drag force in hypersonic shock tunnels. Ulbrich [13] investigated a load diagram technique for strain-gauge balances in wind tunnels, benefiting from the experimental and practical applications in aerodynamic testing. Bardera [14] investigated balance concepts specifically tailored for UAVs (Unmanned Aerial Vehicles), providing a detailed explanation of the calibration process and force measurements on a model designed and tested at INTA. These vehicles often experience low aerodynamic loads due to their small dimensions and low flight range, which is a challenge that becomes even more significant as the dimensions of these vehicles decrease, as seen in smaller UAVs and Micro Air Vehicles (MAVs) [15,16]. In these cases, maximum aerodynamic loads are typically limited to 3–4 Newtons, for which commercial balances are generally unavailable. Standard balance systems lack the necessary sensitivity and precision to measure such small forces accurately, resulting in limited options for effective force measurement in MAV applications.

Due to the absence of commercially available balances suitable for these low load ranges, it is essential to design, manufacture, and precisely calibrate a prototype. Such a prototype must be engineered with high sensitivity to reliably measure forces in this low range, ensuring accurate aerodynamic data collection for MAVs and other small-scale UAVs. This approach addresses the need for high-resolution force measurements in low-Reynolds-number environments, facilitating advancements in MAV performance evaluation and aerodynamic research.

The three-component external balance discussed in this paper was specifically designed and built by the Experimental Aerodynamics Area of INTA to measure aerodynamic forces on Micro Aerial Vehicles (MAVs) in a wind tunnel [17,18]. The load-sensing elements used in this balance are high-precision strain gauge load cells, renowned for their excellent repeatability and linearity. The geometric design of the load-sensing system allows for complete separation and independent measurement of the three key components of aerodynamic loading, namely, lift force, aerodynamic drag force, and pitching moment. The complete balance calibration process is detailed in the next sections, including the mathematical formulation used to obtain the calibration matrix, an analysis of interactions between the force components, and an evaluation of the uncertainties associated with the external balance.

2. External Balance Prototype

Figure 1 shows an overview of the external balance design, illustrating the three load cells (LC − 1, LC − 2, and LC − 3) together with the different mechanisms employed for measuring lift force (L), aerodynamic drag force (D), and pitching moment (M_y).

This prototype will consist of a metallic structure composed of several mechanisms, designed to isolate and measure the forces involved. These mechanisms form the core components of the mechanical balance, facilitating accurate force measurements. The instrumentation of the external balance uses three piezoresistive sensors, specifically, three bending load cells, fixed to various mechanisms, bearing, and bushing, enabling the measurement of lift, aerodynamic drag, and pitching moment. All components that constitute the 3-component external balance are a rectangular base, three mechanisms (1, 2, and 3), a balancing counterweight, three load cells ($LC-1$, $LC-2$, and $LC-3$), two load cell supports, load cell locking systems, ball bearings and bushings, component "U", a bearing assembly, and a rod. The joints of the different mechanisms are formed by a set of ball bearings with bushings, allowing the forces in the X (aerodynamic drag) and Z (lift) axes to be properly transmitted to the load cells independently. Thus, during operation of the system, due to the lift force of the MAV in the vertical direction, mechanism 1, to which the model is attached, moves in the Z direction and forces mechanism 3 to rotate around the fixed joint. Mechanism 3 creates a force that generates a state of bending loads on the

load cell ($LC-3$) and thus the lift force is measured. In the case of the drag force on the MAV in the X direction, the force is transmitted from mechanism 1 through mechanism 2. Commercial load cells with a measurement range of 200 g ($LC-1$ and $LC-3$) and 1000 g ($LC-2$) were used.

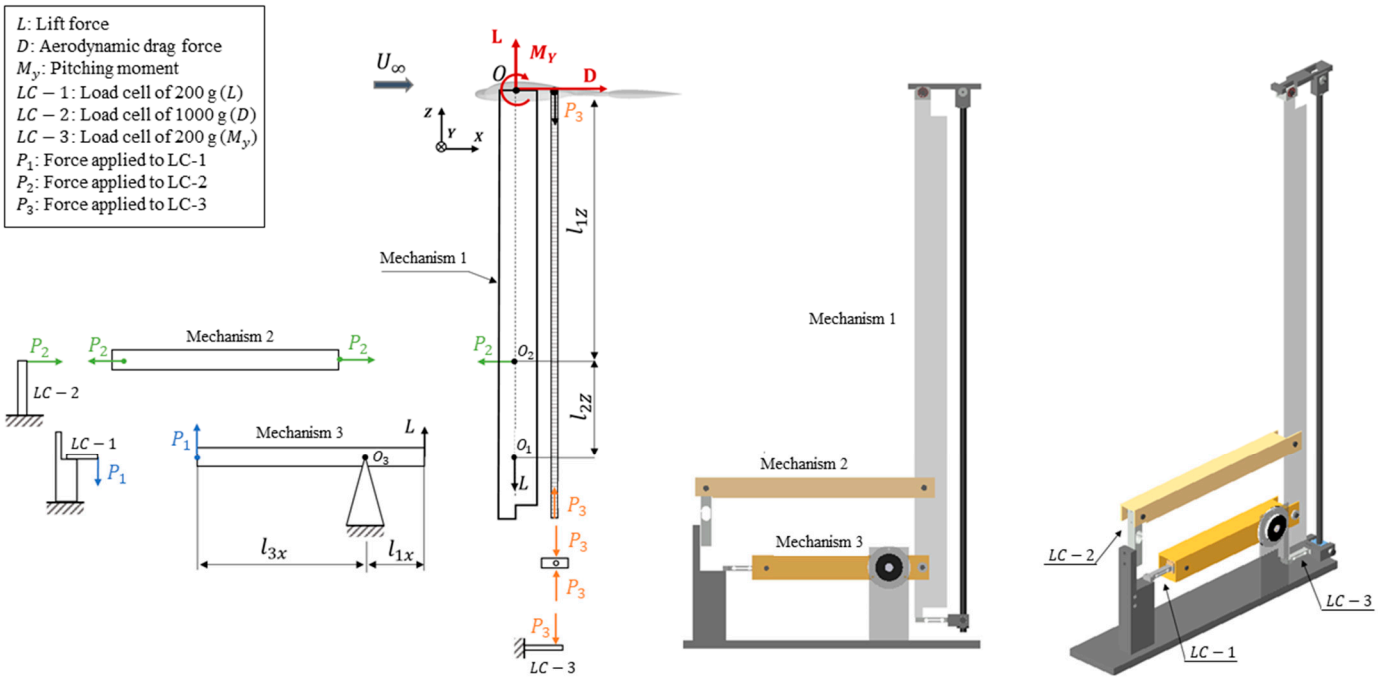

Figure 1. Diagram of the forces generated in the external balance (**left**) and 3D balance design with the position of the mechanisms and load cells (**right**).

Figure 2 shows the junction between the load cell for measuring lift ($LC-2$) and mechanism 3. The load cell is aligned in the same direction as mechanism 3 (in X-axis) and is interconnected through a combination of two ball bearings (bearing A) and bushings (A.1, A.2, and A.3). The component ''B'' is meticulously crafted to facilitate the integration between the bearing assembly and the load cell within mechanism 3. To ensure controlled movement, the opposing side of the load cell is intentionally immobilized, allowing only rotational motion at the junction with mechanism 3.

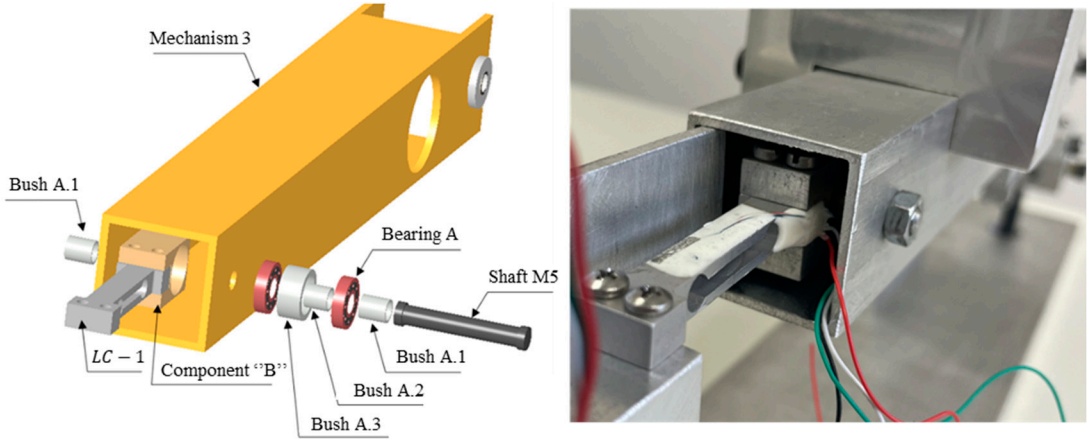

Figure 2. 3D view (**left**) and manufactured assembly (**right**) for the lift measurement.

Figure 3 illustrates the connection between the $LC-2$ load cell, utilized for measuring aerodynamic drag force, and mechanism 2. The $LC-2$ load cell is oriented perpendicularly to mechanism 2 and affixed to it via a set of 4 ball bearings (bearing C) and bushings (B.1). Similar to the previous case, one end of the load cell remains fixed to prevent undesirable movement (fixed to the support), allowing controlled motion within the bearing section.

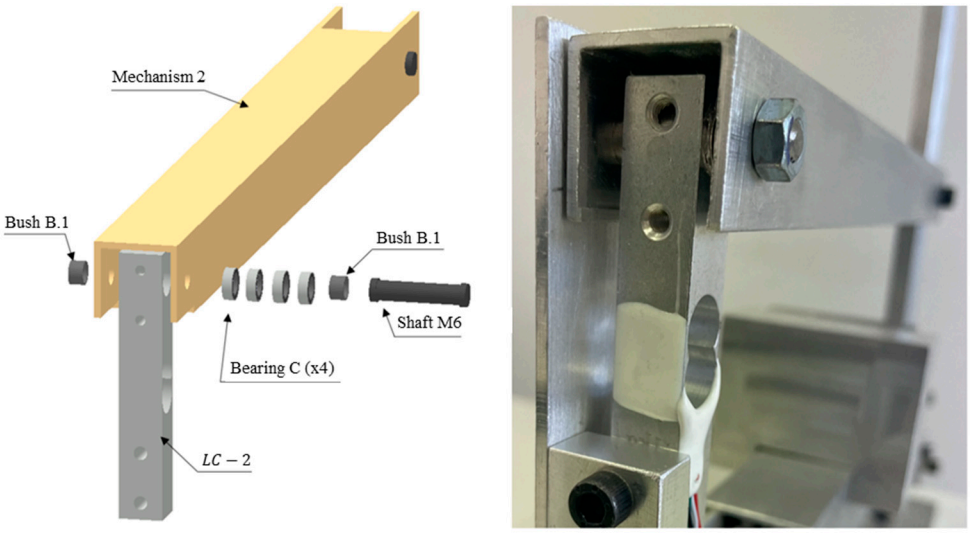

Figure 3. 3D view (**left**) and manufactured assembly (**right**) for the drag measurement.

Figure 4 shows the assembly required to measure the pitching moment (M_y). The load cell ($LC-3$) is positioned horizontally, in the X-axis direction. The assembly involves a bearing assembly (bearing D) and bushings (C.1), enabling rotational movement on one side of the load cell while keeping the other side stationary to prevent unintended motion (fixed to the mechanism 1).

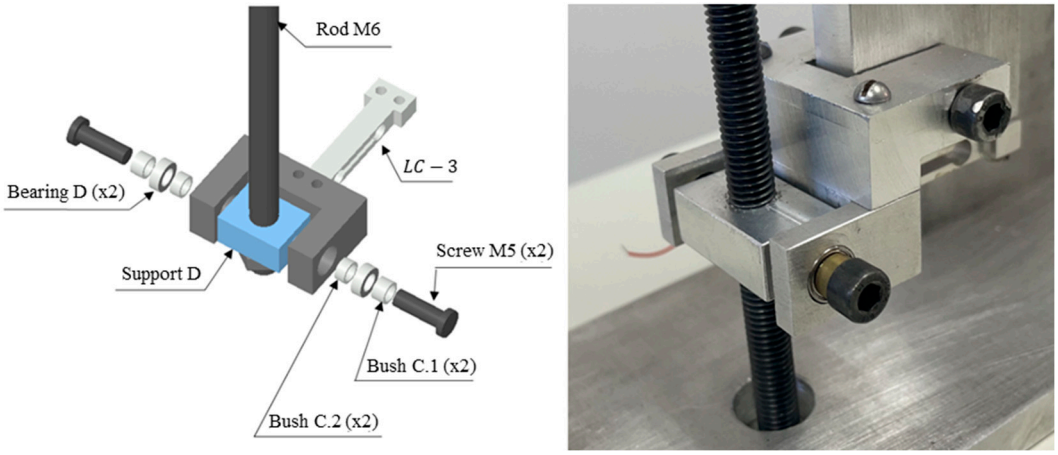

Figure 4. 3D view (**left**) and manufactured assembly (**right**) for the pitching moment measurement.

Figure 5 shows the junction of the external balance with the wind tunnel model, including the components required for adjusting the position of the model. The component ''U" enables the wind tunnel model to rotate along the Y-axis, while the bearing assembly allows adjusting the angle of attack (α).

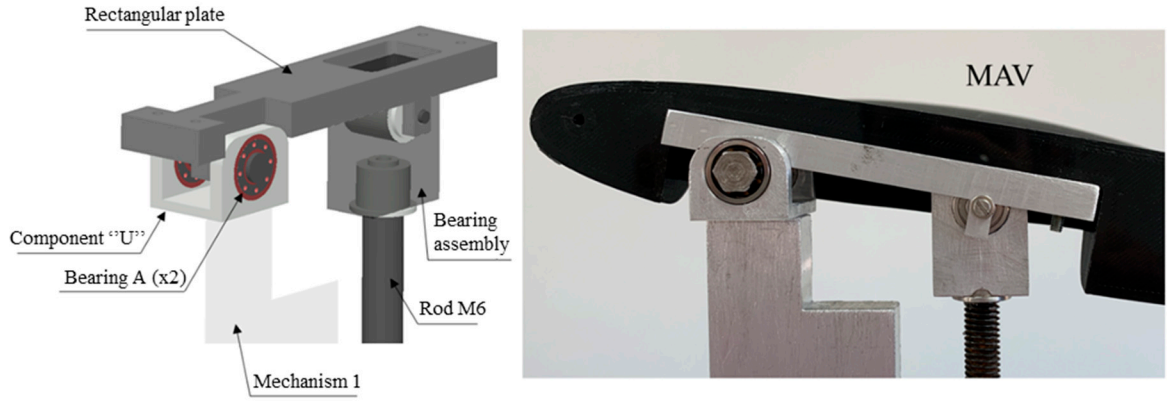

Figure 5. 3D view (**left**) and manufactured assembly (**right**) corresponding to the junction between the external balance and the wind tunnel model.

3. Force Measurements with Balance

When the balance is loaded with a load vector or state of load $[F_L]$, the resulting output signal is measured to generate the matrix $[F_R]$. These matrices can be related by the following expression (1) [19]:

$$[F_R] = [K][F_L] \tag{1}$$

where $[K]$ is the calibration matrix and the subscripts "R" and "L" are indicating reading and applied load, respectively. Measured forces will be given by the recorded signal in the load cells, but when a pure load is applied, all load cells record a signal, mainly due to misalignments and deformations of the balance, producing an error called the interaction load effect. The balance equation gives applied loads as a function of the measured signal using the following formula:

$$[F_L] = [E][F_R] \tag{2}$$

where $[E]$ is the evaluation matrix, calculated as $[E] = [K]^{-1}$.

This equation is used during the wind tunnel tests so that applied loads are unknown, output signals are measured, and matrix A is previously determined using the calibration process. Usually, in practice, forces acting on balance are given by the following matrix expression:

$$[F] = [A][U] + [R] \tag{3}$$

where $[F]$ is the force matrix, $[A]$ is the unknown matrix to be determined by calibration, $[U]$ is the output signals matrix containing the output of the three load cells, and finally, $[R]$ is the residual matrix of the fitting mathematical model used.

The forces acting on the external 3-component balance can be expressed as a function of the output voltages of the 3 load cells by the following second-order polynomial expression:

$$F_i = \sum_{j=1}^{N} A_{ij}U_j + \sum_{j=k}^{N}\sum_{k=1}^{N} A_{ijk}U_jU_k + R_i \tag{4}$$

where F_i is the force or moment of the balance at position "i" within the matrix of forces and moments, U_j are the output voltages of the load cells ($j = 1, 2, 3$) and the term A_{ij} represents the linear terms of the mathematical model. Moreover, A_{ijk} corresponds to the second-order contributions, and R_i is the residual or fit error. The upper index of the summation is $N = 3$, since there are only 3 output signals from the load cells.

The generic development of a force or moment component, resulting from a combination of the 3 output voltage signals recorded in the acquisition system, is detailed below. Therefore, Expression (4) is broken down into first-order linear terms and up to second-order terms (quadratic and cross terms).

$$F_i = A_{i1}U_1 + A_{i2}U_2 + A_{i3}U_3 \quad + \quad \begin{matrix} A_{i11}{U_1}^2 \\ A_{i22}{U_2}^2 \\ A_{i33}{U_3}^2 \end{matrix} \quad + \quad \begin{matrix} A_{i21}U_2U_1 + A_{i31}U_3U_1 \\ A_{i32}U_3U_2 \end{matrix} \quad + \quad R_i \tag{5}$$

⇩ Linear terms ⇩ Quadratic terms ⇩ Cross-terms ⇩ Residual

Normally, the forces and moments acting on the balance are given by the following expression, in matrix form:

$$[F] = [A][U] + [R] \tag{6}$$

where $[F]$ is the matrix of forces and moments, $[A]$ is the matrix to be obtained by calibration, $[U]$ is the matrix of output voltages of the 3 load cells, and finally, $[R]$ is the residual matrix. In general, several hundreds of load cases are necessary to determine the matrix $[A]$ to be representative of the behavior of the balance. The structure of the matrix terms corresponding to each matrix is shown below, together with the dimensions of each matrix, taking into account that the number of load cases is $n = 200$. The matrix of forces and moments $[F]$ is defined as follows:

$$[F]_{3xn} = \begin{pmatrix} F_{x,1} & F_{x,2} \cdots & F_{x,n} \\ F_{z,1} & F_{z,2} \cdots & F_{y,n} \\ M_{y,1} & M_{y,2} \cdots & M_{y,n} \end{pmatrix} \tag{7}$$

This matrix has a dimension of $3 \times n$ due to the fact that the balance only measures the force in the X direction (F_x), the force in the Z direction (F_z), and the moment on the Y axis (M_y). The matrix $[F]$ has units of grams (g) for forces and grams per meter (g·m) for momentum, for calibration purposes, although forces should be converted to Newtons (N) and pitching moments to (N·m), as corresponding to SI units. The calibration matrix $[A]$ will present the following dimension:

$$[A]_{3x9} = \begin{pmatrix} A_{1,1} & A_{1,2} & A_{1,3} & A_{1,4} & A_{1,5} & A_{1,6} & A_{1,7} & A_{1,8} & A_{1,9} \\ A_{2,1} & A_{2,2} & A_{2,3} & A_{2,4} & A_{2,5} & A_{2,6} & A_{2,7} & A_{2,8} & A_{2,9} \\ A_{3,1} & A_{3,2} & A_{3,3} & A_{3,4} & A_{3,5} & A_{3,6} & A_{3,7} & A_{3,8} & A_{3,9} \end{pmatrix} \tag{8}$$

The output signal matrix $[U]$ will be composed of linear, quadratic, and cross terms to solve the second-order equation of the balance forces. Therefore, this matrix would have a dimension of $9 \times n$, where the 9 rows are arranged such that the linear terms are in the first 3 rows, the quadratic terms in the next 3 rows, and finally, the cross terms in the last 3 rows, such that:

$$[U]_{9xn} = \begin{pmatrix} U_{1,1} & U_{1,2} & U_{1,3} & U_{1,4} & \ldots & U_{1,n} \\ U_{2,1} & U_{2,2} & U_{2,3} & U_{2,4} & \ldots & U_{2,n} \\ U_{3,1} & U_{3,2} & U_{3,3} & U_{3,4} & \ldots & U_{3,n} \\ U_{1,1}^2 & U_{1,2}^2 & U_{1,3}^2 & U_{1,4}^2 & \ldots & U_{1,n}^2 \\ U_{2,1}^2 & U_{2,2}^2 & U_{2,3}^2 & U_{2,4}^2 & \ldots & U_{2,n}^2 \\ U_{3,1}^2 & U_{3,2}^2 & U_{3,3}^2 & U_{3,4}^2 & \ldots & U_{3,n}^2 \\ U_{1,1}U_{2,1} & \ldots & \ldots & & \ldots & U_{1,n}U_{2,n} \\ U_{2,1}U_{3,1} & \ldots & \ldots & & \ldots & U_{2,n}U_{3,n} \\ U_{1,1}U_{3,1} & \ldots. & & & \ldots & U_{1,n}U_{3,n} \end{pmatrix} \tag{9}$$

Finally, the residual matrix $[R]$ is defined in the following expression with a dimension of $[3 \times n]$:

$$[R]_{3xn} = \begin{pmatrix} R_{1,1} & R_{1,2} & R_{1,3}R_{1,4} & \ldots & R_{1,n} \\ R_{2,1} & R_{2,2} & R_{2,3}R_{2,4} & \ldots & R_{2,n} \\ R_{3,1} & R_{3,2} & R_{3,3}R_{3,4} & \ldots & R_{3,n} \end{pmatrix} \tag{10}$$

To obtain the matrix A an estimator of the force matrix $[\hat{F}]$ is defined as follows:

$$[\hat{F}] = [A][U] \tag{11}$$

So that the residual matrix is given as follows:

$$[R] = [F] - [\hat{F}] \tag{12}$$

The matrix $[A]$ is obtained by multivariate linear regression (linear in parameters and nonlinear in variables), resolving it by the method of least squares in matrix form. The problem solution is to find the matrix with the minimum square error, and multiplying both sides of the equation by $[U]^T$, we obtain the following equation:

$$[\hat{F}][U]^T = [A][U][U]^T \tag{13}$$

and finally, the matrix $[A]$ is as follows:

$$[A] = [\hat{F}][U]^T \left([U][U]^T\right)^{-1} \tag{14}$$

where T and -1 indicate transpose matrix and inverse, respectively.

4. Balance Calibration

The main objective of the calibration process is to get experimental information for the computation of the matrix $[A]$.

The static calibration of the external balance required the design and fabrication of a calibration bench (Figure 6) composed of a structure outside the balance, a central body, pulleys, wires, supports, and weights. The central body is formed by a set of metallic parts located around the balance (Figure 6B). First, 2 circular pieces are placed, one on each side of the symmetry axis of the balance to generate the pitching moment, followed by 2 square pieces to generate the lift and drag. The diameter of the circular pieces was 4 cm based on the expected pitching moment, and the area of the square pieces was 4×4 cm^2 with a hole inside to house a bearing. Additionally, 4 holes were made, one on each face of the piece, aligned with the symmetry axis of the balance, allowing the application of loads in the lift and drag directions. The outer structure (Figure 6C) was used to fix the pulleys (6 in total), while the weights were placed on top of the supports, which in turn were connected to the central body with wires. Figure 6B shows an example of combined load application (positive drag force, $+D$, positive lift force, $+L$, and positive pitching moment, M_y).

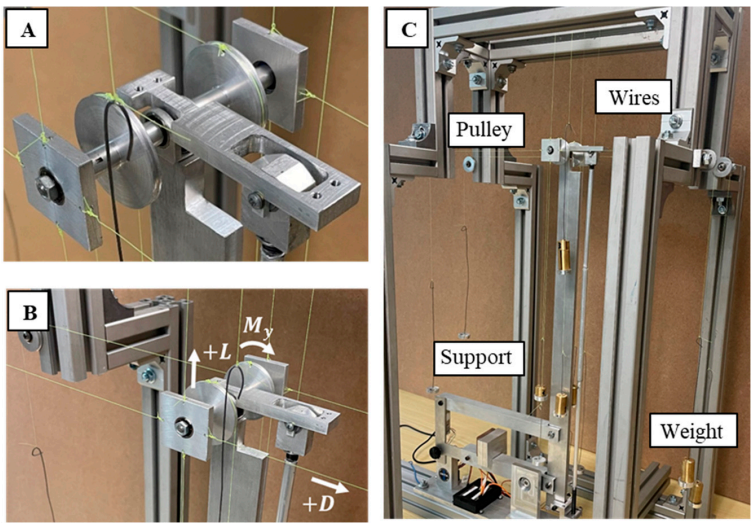

Figure 6. (**A**) Body, (**B**) 3 directions, and (**C**) components for the calibration process.

Since the external balance prototype was designed with the objective of measuring 3 components (L, D , and M_y), loads in 3 different directions must be applied during the calibration process. The selected loads were pure loads (in a single direction) and combined loads (in 2 directions). Figure 7 shows a diagram of the central body with the application load points (12 in total) and the direction of the aerodynamic components based on the balance axes.

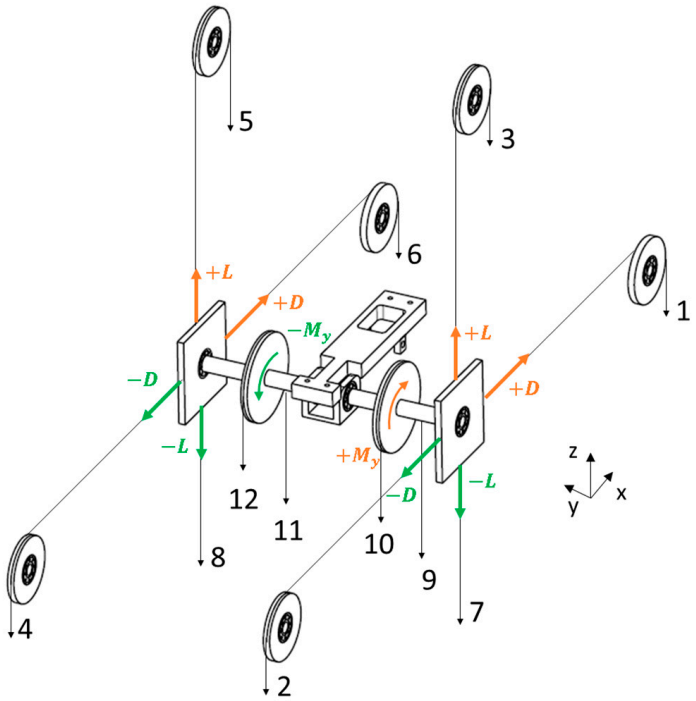

Figure 7. Diagram of directions of the measured components. Orange color indicates the positive forces, while the green color indicates negative forces.

In the calibration process, a maximum load (F_{max}) and 2 intermediate loads ($1/3F_{max}$ and $2/3F_{max}$) are selected. Thus, in each loading case, there will be 7 measurement points, corresponding to the loading phase (zero, $1/3F_{max}$, $2/3F_{max}$, and F_{max}) and the unloading phase ($2/3F_{max}$, $1/3F_{max}$, and zero).

Since the forces expected during the tests with the balance will vary depending on the direction of application, the loads applied in the lift direction (Z-axis) will be greater than the loads applied in the drag direction (Y-axis). To evaluate the forces and the moment, weights of 35 g and 77 g are used. For instance, when loads are applied to points 3 and 5, the balance is subjected to a pure force in the $+Z$ direction, generating a positive lift force (orange arrows in Figure 8). Conversely, when loads are applied to points 7 and 8, the pure force is generated in the $-Z$ direction (green arrows), creating negative lift. To generate a pure force in the $\pm X$ direction, the same procedure as before is followed, but 35 g weights are used. By applying a load in the $+X$ direction, the balance is subjected to a pure positive drag force according to the balance axes (orange arrows in Figure 8). Conversely, if the load is applied in the $-X$ direction, the pure drag force is negative (green arrows). The following tables show an example of load application for the lift force in the $+Z$ direction (Table 1), generating a positive force according to the balance axes, and for the aerodynamic drag force in the $-X$ direction (Table 2), generating a negative force according to the balance axes.

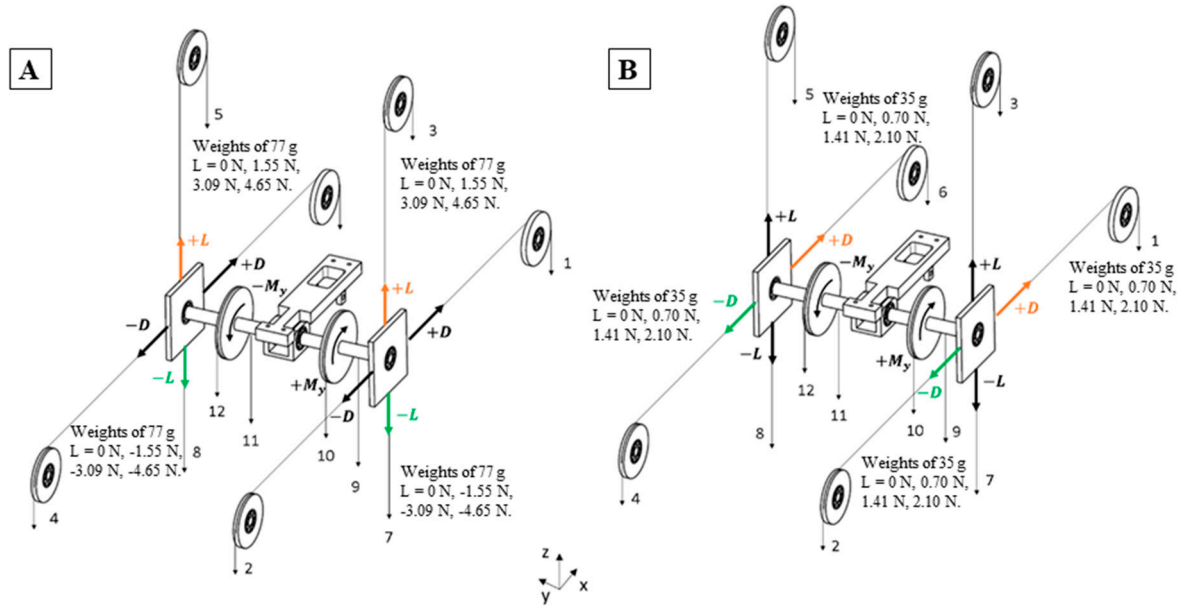

Figure 8. (**A**) Loads to generate pure lift and (**B**) pure aerodynamic drag force.

Table 1. Loading and unloading phase to generate pure lift force $+L$

Loads	*P*.3(+*L*)	*P*.5(+*L*)	*P*.7(−*L*)	*P*.8(−*L*)	*L*(*N*)	*D*(*N*)	M_Y(*Nm*)
0	0	0	0	0	0	0	0
+1/3L_{max}	1 × 77 g	1 × 77 g	0	0	1.54	0	0
+2/3L_{max}	2 × 77 g	2 × 77 g	0	0	3.09	0	0
+L_{max}	3 × 77 g	3 × 77 g	0	0	4.64	0	0
+2/3L_{max}	2 × 77 g	2 × 77 g	0	0	3.09	0	0
+1/3L_{max}	1 × 77 g	1 × 77 g	0	0	1.54	0	0
0	0	0	0	0	0	0	0

Table 2. Loading and unloading phase to generate pure drag force $-D$

Loads	*P*.2(−*D*)	*P*.4(−*D*)	*P*.1(+*D*)	*P*.6(+*D*)	*L*(*N*)	*D*(*N*)	M_Y(*Nm*)
0	0	0	0	0	0	0	0
−1/3D_{max}	1 × 35 g	1 × 35 g	0	0	0	−0.70	0
−2/3D_{max}	2 × 35 g	2 × 35 g	0	0	0	−1.41	0
−D_{max}	3 × 35 g	3 × 35 g	0	0	0	−2.10	0
−2/3D_{max}	2 × 35 g	2 × 35 g	0	0	0	−1.41	0
−1/3D_{max}	1 × 35 g	1 × 35 g	0	0	0	−0.70	0
0	0	0	0	0	0	0	0

To generate a pure pitching moment (see Figure 9), loads will be applied to points 9, 10, 11, and 12 of the circular pieces in such a way that a positive or negative moment is generated depending on the applied loads. Additionally, loads are applied to points 3 and 5 to generate force in the $+Z$ direction and counterbalance them with the loads applied to the circular pieces so that no lift is generated and only the pitching moment is generated. Figure 9 shows an example for generating $2/3M_{ymax}$ and Table 3 indicates the loading and unloading phase to generate pure positive pitching moment, $+M_y$.

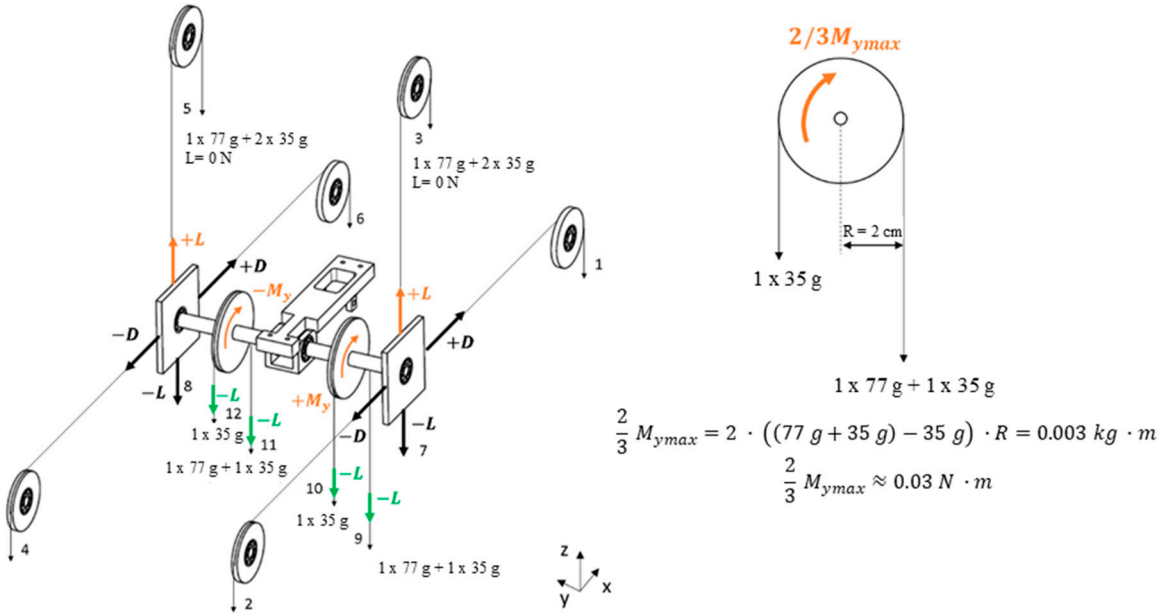

Figure 9. Loads to generate pure pitching moment.

Table 3. Loading and unloading phase to generate pure pitching moment $+M_y$

Loads	*P*.3(+*L*)	*P*.5(+*L*)	*P*.9	*P*.10	*P*.11	*P*.12	*L*(*N*)	*D*(*N*)	M_y(*Nm*)
0	0	0	0	0	0	0	0	0	0
+1/3M_{ymax}	1 × 77 g + 1 × 35 g	1 × 77 g + 1 × 35 g	1 × 77 g	1 × 35 g	1 × 77 g	1 × 35 g	−0.0007	0	0.016
+2/3M_{ymax}	1 × 77 g + 2 × 35 g	1 × 77 g + 2 × 35 g	1 × 77 g + 1 × 35 g	1 × 35 g	1 × 77 g + 1 × 35 g	1 × 35 g	−0.009	0	0.037
+M_{ymax}	1 × 77 g + 2 × 35 g	1 × 77 g + 2 × 35 g	1 × 77 g + 2 × 35 g	1 × 35 g	1 × 77 g + 2 × 35 g	1 × 35 g	−0.704	0	0.044
+2/3M_{ymax}	1 × 77 g + 2 × 35 g	1 × 77 g + 2 × 35 g	1 × 77 g + 1 × 35 g	1 × 35 g	1 × 77 g + 1 × 35 g	1 × 35 g	−0.008	0	0.037
+1/3M_{ymax}	1 × 77 g + 1 × 35 g	1 × 77 g + 1 × 35 g	1 × 77 g	1 × 35 g	1 × 77 g	1 × 35 g	−0.0007	0	0.016
0	0	0	0	0	0	0	0	0	0

A. Data acquisition

The balance is composed of 3 load cells, each consisting of 4 strain gauges connected by a Wheatstone bridge that will provide 3 output electrical signals with voltages (U_1, U_2, and U_3). These electrical signals are read using HX711 modules (A/D converter) connected to the Arduino microcontroller, which was powered by 5 V voltage. For each load application case, a record of the 3 electrical signals is obtained for a recording time of 10 s, with a sampling frequency of 10 Hz, resulting in 100 equally spaced measurements over time. According to the manufacturer's specifications, the load cells have an error equal to $\epsilon = 0.05\% = 0.0005 = 5{\cdot}10^{-4}$, which is much smaller than the resolution of the converter (2^{24} = 16,777,216), and therefore, the acquisition of the scale signals is verified. The HX711 A/D converter amplifies the analog output signal of the load cell with a gain of 128. The signals will then be digitized and expressed in bits.

B. Matrix [A]

The calibration matrix $[A]$ presents the following form:

$$[A]_{3x9} = \begin{bmatrix} -5.536^{-4} & 2.341^{-6} & -4.469^{-6} & 8.624^{-12} & 8.316^{-13} & 2.999^{-11} & -4.278^{-12} & 8.506^{-14} & 8.161^{-14} \\ 3.929^{-6} & -8.892^{-5} & -8.773^{-6} & -9.280^{-13} & 1.518^{-13} & -4.551^{-12} & 7.492^{-14} & 1.371^{-13} & 2.054^{-13} \\ 1.321^{-8} & -5.923^{-8} & 5.733^{-6} & -1.746^{-14} & -2.649^{-15} & -8.931^{-14} & 5.606^{-15} & -2.731^{-15} & 1.391^{-14} \end{bmatrix} \quad (15)$$

C. Balance interactions

The study of force interactions in balance measurements allows for an assessment of force decoupling achieved through the mechanical design of the balance.

First-order interactions:

The linear terms correspond to first-order interactions, which represent misalignments due to fabrication tolerances and the mechanical assembly of balance components. The terms A_{ij} with $i = j$ indicate the balance's sensitivity to the three types of loads being measured. In contrast, elements A_{ij} with $i \neq j$ are the linear interaction coefficients that account for the influence of a load that does not produce an output signal. The linear part of the A matrix is as follows:

$$[A]_{linear} = \begin{bmatrix} -5.536 \cdot 10^{-4} & 2.341 \cdot 10^{-6} & -4.469 \cdot 10^{-6} \\ 3.929 \cdot 10^{-6} & -8.892 \cdot 10^{-5} & -8.773 \cdot 10^{-6} \\ -1.681 \cdot 10^{-8} & -5.923 \cdot 10^{-8} & 5.733 \cdot 10^{-6} \end{bmatrix} \quad (16)$$

The sensitivity S_i of each load cell, as installed in the balance, corresponds to the inverse of the diagonal elements of matrix [A]. It is defined as the variation in output signal produced by a variation in input load and is given as follows:

$$S_i = \frac{\Delta U_i}{\Delta F_i} = \frac{1}{A_{ii}} (i = 1, 2, 3) \quad (17)$$

Table 4 shows the sensitivity of each load cell.

Table 4. Sensitivity of load cells.

Load Cell i	Sensitivity	Units	Relative Sensitivity
1	$-1.806 \cdot 10^{3}$	Bit/g	1
2	$-1.124 \cdot 10^{4}$	Bit/g	6.226
3	$1.744 \cdot 10^{5}$	Bit/g·m	$-9.657 \cdot 10^{1}$

The negative sign in the sensitivity indicates a negative slope of the sensitivity curve, as the load cells measure negative bending moments. The type of load cells used in this balance can measure both negative and positive bending moments.

From the sensitivity values, it is observed that the sensitivity of load cell 2 is approximately 6 times that of load cell 1, while the sensitivity of load cell 3 is 97 times higher than that of load cell 1.

To understand the contribution of each component to the overall load, the balance is treated as a "black box" sensor from a global perspective. In this approach, applied loads excite the balance, which then responds with output signals. The following analysis examines a representative case where three types of loads—lift, drag, and pitching moment—are applied to the balance. The values of these loads lie within the mid-range of the measurement spectrum, and the resulting data are analyzed to assess their impact.

$$[F]_{real\ load} = \begin{bmatrix} L(\mathrm{g}) \\ D(\mathrm{g}) \\ M(\mathrm{g \cdot m}) \end{bmatrix}_{real\ load} = \begin{bmatrix} 309.2 \\ 141.1 \\ 3.07 \end{bmatrix} \quad (18)$$

Estimated loads from the measured signals with linear term (first-order approximation) are as follows:

$$[\hat{F}] = [A][U] = \begin{bmatrix} -5.536 \cdot 10^{-4} & 2.341 \cdot 10^{-6} & -4.469 \cdot 10^{-6} \\ 3.929 \cdot 10^{-6} & -8.892 \cdot 10^{-5} & -8.773 \cdot 10^{-6} \\ -1.681 \cdot 10^{-8} & -5.923 \cdot 10^{-8} & 5.733 \cdot 10^{-6} \end{bmatrix} \begin{bmatrix} -5.656 \cdot 10^{5} \\ -1.557 \cdot 10^{6} \\ 5.505 \cdot 10^{5} \end{bmatrix} \quad (19)$$

$$[\hat{F}] = \begin{bmatrix} L(\mathrm{g}) \\ D(\mathrm{g}) \\ M(\mathrm{g \cdot m}) \end{bmatrix} = \begin{bmatrix} 304.0 \\ 132.5 \\ 3.2 \end{bmatrix} \quad (20)$$

For instance, lift L is given by the following expression:

$$L = A_{11} \cdot U_1 + A_{12} \cdot U_2 + A_{13} \cdot U_3 \quad (21)$$

and dividing the right part by the dominant term, result,

$$\frac{L}{A_{11} \cdot U_1} = 1 + \frac{A_{12} \cdot U_2}{A_{11} \cdot U_1} + \frac{A_{13} \cdot U_3}{A_{11} \cdot U_1} \quad (22)$$

and in the same manner, for drag (D) and pitching moment (M_y), the contributions to the total load are obtained (Table 5).

Table 5. Contributions to the total load cells for first-order interactions.

		First-Order Normalized Contributions		
i	$A_{ij} \cdot U_j / A_{ii} \cdot U_i$	j = 1	j = 2	j = 3
1	$A_{1j} \cdot U_j / A_{11} \cdot U_1$	1	$-1.16 \cdot 10^{-2}$	$-7.85 \cdot 10^{-3}$
2	$A_{2j} \cdot U_j / A_{22} \cdot U_2$	$-1.60 \cdot 10^{-2}$	1	$-3.48 \cdot 10^{-2}$
3	$A_{3j} \cdot U_j / A_{33} \cdot U_3$	$3.01 \cdot 10^{-3}$	$2.92 \cdot 10^{-2}$	1

It can be observed that the primary component is dominant, as the diagonal elements are equal to unity, while the other contributions are on the order of $O\left(10^{-2}\right)$.

$$\frac{L}{A_{11} \cdot U_1} \approx 1 + O\left(10^{-2}\right) \quad (23)$$

$$\frac{D}{A_{22} \cdot U_2} \approx 1 + O\left(10^{-2}\right) \quad (24)$$

$$\frac{My}{A_{33} \cdot U_3} \approx 1 + O\left(10^{-2}\right) \quad (25)$$

Second-order interactions:

Second-order interactions arise from the elastic deformations of the balance structure. The elements A_{ijk}, when $j \neq k$ correspond to interaction products of load components that would not typically produce an output signal, while elements with $j = k$ reflect second-order interactions due to nonlinearity in sensitivity. The results of the second-order interactions, as shown in the table, are of the order $\mathrm{O}\left(10^{-2}\right)$, similar to the first-order interactions. These interactions are considered to ensure a more accurate adjustment of the balance. Table 6 indicates the contributions to the total load cells for second-order interactions.

D. Residuals

Table 7 shows the non-dimensional mean residual values $\overline{R_{F_i}}(\%FS)$ defined as follows:

$$\overline{R_{F_i}}(\%FS) = \frac{R_{F_i}}{FS_{F_i}} \cdot 100 \quad (26)$$

where R_{F_i} is the residual for each component measured with the balance (F_i) and FS is the full scale corresponding to each of them, which will be different for each component. Then, for the lift component, the full scale will be equal to $FS_L = 600$ g, while for the drag component, it will be $FS_D = 200$ g and for the pitching moment, it will be $FS_{M_y} = 8$ g·m. Moreover, Table 7 presents the non-dimensional standard deviation $s_{F_i}(\%FS)$ of the residuals for each component measured with the balance (F_i), which represents the mean square error of the fit model as follows:

$$s_{F_i}{}^2 = \frac{1}{n-p}\left[[R]\,[R]^T\right]_{ii} \; with\; i = 1,2,3; \quad and \quad s_{F_i} = \sqrt{s_{F_i}{}^2} \tag{27}$$

where $n - p$ are the freedom degrees with $p = 9$.

Table 6. Contributions to the total load cells for second-order interactions.

	$A_{ijk}\cdot U_j\cdot U_k / A_{ii}\cdot U_i$						
i	$j=1,\ k=1$	$j=2,\ k=2$	$j=3,\ k=3$	$j=2,\ k=1$	$j=3,\ k=1$	$j=3,\ k=2$	Total
1	$8.81\cdot10^{-3}$	$6.43\cdot10^{-3}$	$2.90\cdot10^{-2}$	$-1.20\cdot10^{-2}$	$-8.45\cdot10^{-5}$	$-2.23\cdot10^{-4}$	$3.19\cdot10^{-2}$
2	$-2.14\cdot10^{-3}$	$2.65\cdot10^{-3}$	$-9.96\cdot10^{-3}$	$4.76\cdot10^{-4}$	$-3.08\cdot10^{-4}$	$-1.27\cdot10^{-3}$	$-1.05\cdot10^{-2}$
3	$-1.77\cdot10^{-3}$	$1.32\cdot10^{-3}$	$-8.58\cdot10^{-3}$	$1.56\cdot10^{-3}$	$2.69\cdot10^{-4}$	$-3.77\cdot10^{-3}$	$-1.09\cdot10^{-2}$

Table 7. Mean values, standard deviation, and uncertainty of residuals for mid-range loads.

F_i	$\overline{R_{F_i}}(\%FS)$	$s_{F_i}(\%FS)$	$U_{\hat{F}_i}(\%FS)$
L	0.518	1.272	2.738
D	−0.124	1.158	2.668
M_y	0.018	0.723	1.700

Several sources of error can affect the performance of the balance, but the uncertainty can be determined by considering that a generic force measurement by the balance equals the real force (applied load) acting on it, minus the corresponding residual.

$$\hat{F}_i = F_{i_{real-load}} - R_i = f\left(F_{i_{real-load}},\ R_i\right) \tag{28}$$

Then, the combined uncertainty can be computed as follows:

$$u^2_{\hat{F}_i} = \left(\frac{\partial f}{\partial F_{i_{real-load}}}\right)^2 u^2_{F_{i_{real-load}}} + \left(\frac{\partial f}{\partial R_i}\right)^2 u^2_{R_i} = u^2_{F_{i_{real-load}}} + u^2_{R_i} \tag{29}$$

The uncertainty in the value of the real load arises because the input of the applied load in the calibration bench does not exactly match the nominal value. This discrepancy is due to the weights used during calibration, which were measured using an analytical balance with a resolution of 1 mg. Additionally, friction in the pulleys, misalignments, and deformations in the mechanical structure of the bench can introduce uncertainties estimated to be on the order of 10^{-2} of the load, as determined during the balance's calibration in the mid-range.

The uncertainty of the residual can be estimated using the standard deviation, calculated from the variance of the residuals. The expanded uncertainty $U_{\hat{F}_i}$ is given by the following equation:

$$U_{\hat{F}_i} = k\cdot u_{\hat{F}_i} \tag{30}$$

where k is the coverage factor, with a value of $k = 2$ for a 95% confidence level. Thus, the result of a measurement with the balance is expressed as follows:

$$F_i = \hat{F}_i \pm U_{\hat{F}_i} \tag{31}$$

E. Verification

The verification process of the external balance involved determining the force matrix $[F]$ measured by the balance using two methods. First, an initial verification was conducted using the same output signals $[U]$ from the calibration (Figures 10A, 11A and 12A), allowing for the calculation of the calibration residual to ensure that it is minimal. Next, a second verification was carried out by applying known loads different from those used during calibration. This approach assesses the balance's accuracy from a global perspective as a "black box" sensor, where the balance is subjected to input loads and responds with output digital signals. In this case, a total of five loads were selected, including both pure and combined loads (Figures 10B, 11B and 12B).

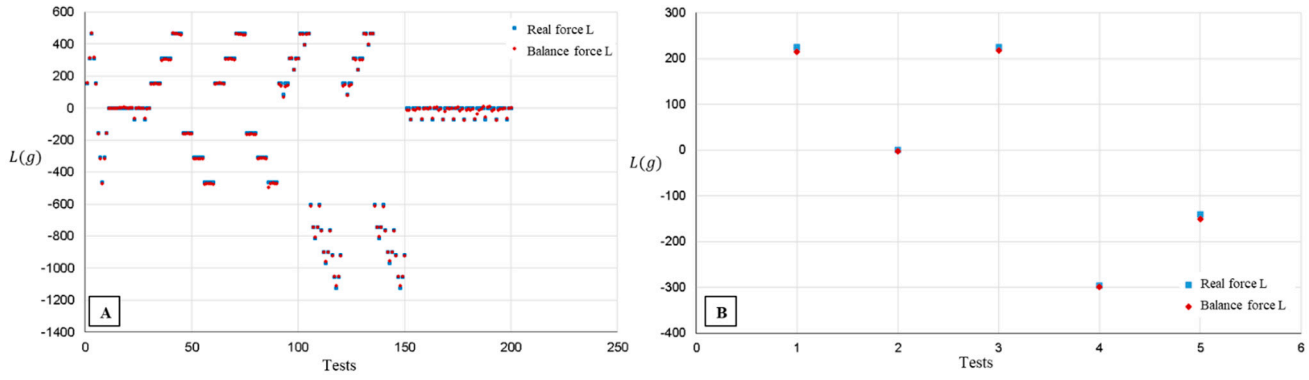

Figure 10. Verification of lift with calibration loads (**A**) and 5 selected loads (**B**).

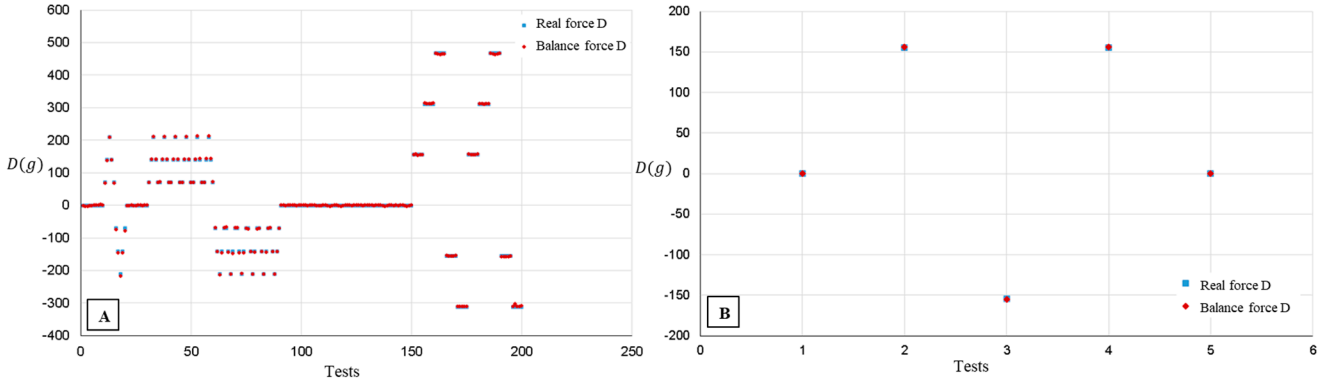

Figure 11. Verification of aerodynamic drag with calibration loads (**A**) and 5 selected loads (**B**).

Figure 10 shows the real lift data, that is, the force matrix $[F]$ with the applied and known loads (blue points) and the lift values measured with the external balance (data in red). It can be observed that the real values are almost identical to the values measured by the external balance in the verification with calibration loads (Figure 10A). However, in the verification with 5 selected loads, there is a small deviation between the real load and the load measured by the balance for the 3 and the 5 load points (1, 3, and 5).

Figures 11 and 12 show the real aerodynamic drag data and pitching moment, respectively, that is, the force matrix $[F]$ with the applied and known loads (blue points) and the values measured with the external balance (data in red). As in the previous case, the real values are practically the same as the values measured by the external balance in the two verifications. Since these components present rather lower values compared to the lift force,

it can be concluded that the deviation is in the allowable range of measurement, and thus the calibration matrix $[A]$ results to be valid for future wind tunnel tests.

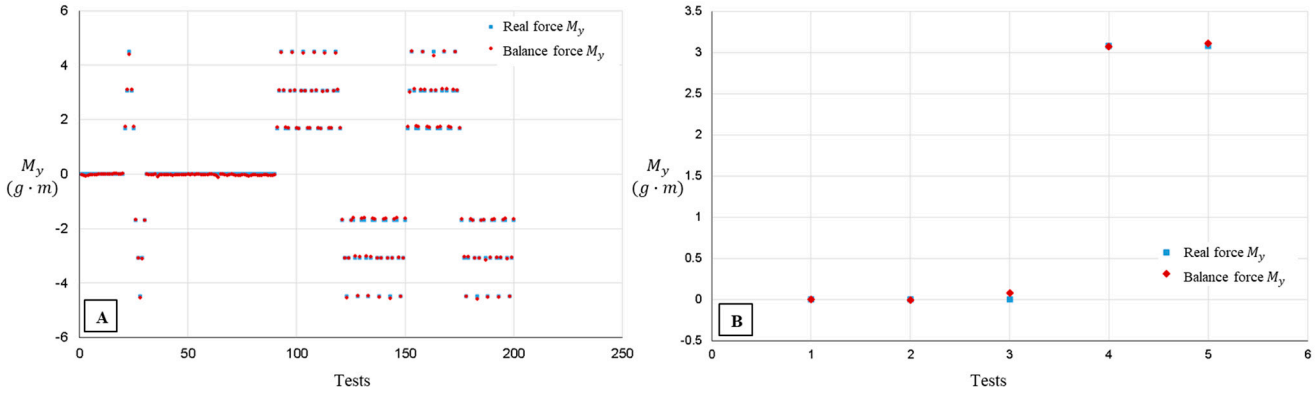

Figure 12. Verification of pitching moment with calibration loads (**A**) and 5 selected loads (**B**).

Table 8 shows the force and moment values that constitute the matrix $[F]$ of real values, that is, the 5 selected load cases, the force, and moment values measured with the balance.

Table 8. Verification with the 5 selected loads.

N°	F_{i_real}			$F_{i\_balance}$		
Case	$L(g)$	$D(g)$	$My(g{\cdot}m)$	$L(g)$	$D(g)$	$My(g{\cdot}m)$
1	225.175	0	0	215.152	0.407	0.001
2	0	154.816	0	−2.380	156.048	−0.004
3	225.175	−154.368	0	216.895	−154.840	0.077
4	−295.46	154.816	3.0798	−299.313	156.284	3.075
5	−140.644	0	3.0798	−151.302	0.425	3.109

The absolute error in the measurement of each component $|\Delta F_i|$ is calculated as follows:

$$|\Delta F_i| = |F_{i\_real} - F_{i\_balance}| \tag{32}$$

where i represents each measured force or moment in each load case.

The relative error of each component in percentage $\varepsilon_{F_i}(\%)$ is defined as follows:

$$\varepsilon_{F_i}(\%) = \frac{|\Delta F_i|}{|F_i|} \cdot 100 \tag{33}$$

Table 9 shows the errors in the measurement of each component and the non-dimensional values according to the full scale (FS).

Table 9. Absolute and relative errors of each load component.

N°	$\lvert\Delta L\rvert(g)$	$\frac{\lvert\Delta L\rvert}{FS_L}(\%)$	$\frac{\lvert\Delta L\rvert}{L}(\%)$	$\lvert\Delta D\rvert(g)$	$\frac{\lvert\Delta D\rvert}{FS_D}(\%)$	$\frac{\lvert\Delta D\rvert}{D}(\%)$	$\lvert\Delta My\rvert(gm)$	$\frac{\lvert\Delta My\rvert}{FS_{My}}(\%)$	$\frac{\lvert\Delta My\rvert}{My}(\%)$
1	10.023	1.670	4.451	0.407	0.203	---	0.001	0.007	---
2	2.380	0.396		1.232	0.616	0.795	0.004	0.045	---
3	8.280	1.380	3.677	0.472	0.236	0.305	0.077	0.967	---
4	3.853	0.642	1.303	1.468	0.733	0.948	0.005	0.059	0.155
5	10.658	1.776	7.578	0.425	0.212	---	0.029	0.362	0.942

5. Conclusions

This paper presents the mechanical design and the calibration process of a 3-component external balance for measuring aerodynamic forces on a Micro Air Vehicle. The entire process, from fabrication to calibration, was carried out at the Experimental Aerodynamics Department of the National Institute for Aerospace Technology (INTA). The balance features a complex metallic structure, utilizing high-precision strain gauge cells strategically placed to measure lift and drag forces and pitching moments. Moreover, the calibration bench built for this external balance is also described, and it is intended for future wind tunnel testing.

Notably, the measurement errors of the external balance obtained during calibration and verified using different loads (from those used in calibration) were low, with maximum errors of 1.78% FS for lift force, 0.73% FS for aerodynamic drag, and 0.98% FS for pitching moment (Table 9). This high level of accuracy ensures reliable results for aerodynamic testing and provides a robust tool for future wind tunnel experiments.

Author Contributions: Conceptualization, R.B., Á.A.R.-S., E.B.B., S.S. and J.C.M.G.; methodology, R.B., Á.A.R.-S., E.B.B., S.S. and J.C.M.G.; software, J.C.M.G. and E.B.B.; validation, R.B., Á.A.R.-S., E.B.B., S.S. and J.C.M.G.; formal analysis, R.B.M, Á.A.R.-S., E.B.B., S.S. and J.C.M.G.; investigation, R.B., Á.A.R.-S., E.B.B., S.S. and J.C.M.G.; resources, J.C.M.G. and E.B.B.; data curation, R.B., Á.A.R.-S., E.B.B., S.S. and J.C.M.G.; writing—original draft preparation, R.B., Á.A.R.-S., E.B.B., S.S. and J.C.M.G.; writing—review and editing, R.B., Á.A.R.-S., E.B.B., S.S. and J.C.M.G.; visualization, R.B.; Supervision, R.B.; project administration, R.B.; funding acquisition, R.B. All authors have read and agreed to the published version of the manuscript.

Funding: This study is partially funded by the "Termofluidodinámica" program 464A 64 1999 14 205 0005 of the Spanish Ministry of Defense with INTA internal code IDATEC S.IGB21001.

Institutional Review Board Statement: Not applicable.

Informed Consent Statement: Not applicable.

Data Availability Statement: Dataset available on request from the authors.

Acknowledgments: The authors would like to thank the staff of the Experimental Aerodynamics department of INTA who participated in the tests presented in this paper.

Conflicts of Interest: The authors declare no conflicts of interest. The funders had no role in the design of this study; in the collection, analyses, or interpretation of data; in the writing of the manuscript; or in the decision to publish the results.

References

1. Gonzalez, M.; Ezquerro, M.J.; Lapuerta, V.; Laveron, A.; Rodriguez, J. Components of a wind tunnel balance: Design and calibration. In *Wind Tunnels and Experimental Fluid Dynamics Research*; Lerner, J.C., Boldes, U., Eds.; InTech: Rijeka, Croatia, 2011. [CrossRef]
2. Vukovic, D.; Samardzic, M.; Vitic, A. Prototype of a Stiff Wind Tunnel Balance with Semiconductor Strain Gauges and Thermocompensation Done by Woftward. In Proceedings of the 26th International Congress of the Aeronautical Sciences, Anchorage, AL, USA, 14–19 September 2008; pp. 1–8.
3. Webster, J.; Hazarian, E. Strain Measurement. In *The Measurement, Instrumentation, and Sensor Handbook*, 1st ed.; Chapter 22; CRC Press: Boca Raton, FL, USA, 1990.
4. Anastasijevic, Z.; Samardzic, M.; Marinkovski, D. *Strain Gauges Based Electromechanical Force Transducers and Their Application in Wind Tunnel Tests*; Scientific Technical Information; Military Technical Institute: Belgrade, Serbia, 2004; Volume 38, ISSN 1820-3418, ISBN 86-81123-07-6.
5. Tavakolpour-Saleh, A.; Setoodeh, A.; Gholamzadeh, M. A novel multi-component strain-gauge external balance for wind tunnel tests: Simulation and experiment. *Sens. Actuators A Phys.* **2016**, *247*, 172–186. [CrossRef]
6. Samardzic, M.; Anastasijevic, Z.; Marinkovski, D.; Curcic, D.; Isakovic, L. *External Six-Component Strain Gauge Balance for Low Speed Wind Tunnels*; Scientific Technical Review; Military Technical Institute: Belgrade, Serbia, 2014; Volume 64, No. 3, pp. 40–46.
7. *AIAA R-091-2003e*; Recommended Practice for Calibration and Use of Internal Strain-Gauge Balances with Application to Wind Tunnel Testing. American Institute of Aeronautics and Astronautics: Reston, VA, USA, 2003; ISBN 978-1-56347-646-4.
8. Monkewitz, M.; Muller, J. *Measuring of Long Tuck Models in a Wind Tunnel with External Balance*; SAE Technical Paper 2008-01-1202; SAE: Warrendale, PA, USA, 2008. [CrossRef]

9. Reis, M.L.C.C.; Castro, R.M.; Mello, O.A.F. Calibration uncertainty estimation of a strain gauge external balance. *Measurement* **2013**, *46*, 24–33. [CrossRef]
10. Morris, M.; Post, S. Force Balance Design for Educational Wind Tunnels. In Proceedings of the ASEE Annual Conference & Exposition, Louisville, KY, USA, 20–23 June 2010; American Society for Engineering Education (ASEE): Washington, DC, USA, 2010.
11. Raush, G.; Castilla, R.; Gamez-Montero, P.; Wojciechowski, J.; Codina, E. Flexible rod design for educational wind balance. *Exp. Tech.* **2013**, *40*, 111–119. [CrossRef]
12. Vadassery, P.; Joshi, D.; Rolim, T.; Lu, F. Design and testing of an external drag balance for a hypersonic shock tunnel. *Measurement* **2013**, *46*, 2110–2117. [CrossRef]
13. Ulbrich, N. Combined load diagram for a wind tunnel strain-gauge balance. In Proceedings of the 27th AIAA Aerodynamics Measurement and Ground Testing Conference, Chicago, IL, USA, 28 June–1 July 2010; Jacobs Technology Inc.: Moffet Field, CA, USA, 2010. [CrossRef]
14. Bardera, R. Unmanned Aircraft Wind Tunnel Testing. In *Advanced UAV Aerodynamics, Flight Stability and Control: Novel Concepts, Theory and Applications*; Chapter, 5, Marques, P., Da Ronch, A., Eds.; John Wiley & Sons Ltd.: Hoboken, NJ, USA, 2017.
15. Cheng, L.; Cheng, C.; Zhou, C.; Zhang, Y.; Wu, J. Flapping rotary wing: A novel low-Reynolds number layout merging bionic features into micro rotors. *Prog. Aerosp. Sci.* **2004**, *146*, 100984. [CrossRef]
16. Phan, H.V.; Park, H.C. Insect-inspired, tailless, hover-capable flapping-wing robots: Recent progress, challenges, and future directions. *Prog. Aerosp. Sci.* **2019**, *111*, 100573. [CrossRef]
17. Bardera, R.; Rodríguez-Sevillano, Á.A.; Barroso Barderas, E.; Matías García, J.C. Computational Sudy of Aerodynamic Effects of the Dihedral and Angle of Attack of Biomimetic Grids Installed on a Mini UAV. *Biomimetics* **2024**, *9*, 12.
18. Barroso Barderas, E.; Bardera Mora, R.; Rodríguez-Sevillano, Á.A.; Matías García, J.C. Numerical Analysis of Bioinspired Tails in a Foxed-Wing Micro Air Vehicle. *Aerospace* **2023**, *10*, 793. [CrossRef]
19. Barlow, J.B.; Rae, W.H.; Pope, A., Jr. *Low Speed-Wind Tunnel Testing*, 3rd ed.; John Wiley & Sons, Ltd.: Hoboken, NJ, USA, 1999.